Journal of Power Sources 455 (2020) 227987

Contents lists available at ScienceDirect

Journal of Power Sources

journal homepage: www.elsevier.com/locate/jpowsour

A high-energy aqueous on-chip lithium-ion capacitor based on interdigital 3D carbon microelectrode arrays

Ebenezer Adelowo, Amin Rabiei Baboukani, Omena Okpowe, Iman Khakpour, Meer Safa, Chunhui Chen, Chunlei Wang *

Department of Mechanical and Materials Engineering, Florida International University, Miami, FL, 33174, United States

HIGHLIGHTS

- An on-chip lithium-ion capacitor based on 3D carbon microelectrodes is presented.
- The capacity of the carbon microelectrodes improved with oxygen plasma treatment.
- $LiFePO_4$ incorporated with the carbon structure to realize a battery-type cathode.
- The device shows areal energy density about 5 times higher than symmetric system.

ARTICLE INFO

Keywords:
Lithium-ion capacitor
On-chip
Carbon microelectromechanical systems
$LiFePO_4$

ABSTRACT

There is a growing interest in the development of high energy on-chip capacitive energy storage units for application in microelectronic devices. Lithium-ion capacitor (LIC) typically comprising battery-type and capacitor-type electrodes offer the opportunity for an improved energy density in capacitive energy storage. In this work, an aqueous on-chip LIC was fabricated using carbon microelectromechanical systems (C-MEMS) technique. Oxygen plasma-treated 3D carbon microelectrode arrays served as the capacitor-type electrode in the LIC, while $LiFePO_4$ integrated on the 3D carbon microelectrode arrays was used as the battery-type cathode. Electrochemical performance evaluation shows that the aqueous on-chip LIC can deliver an areal density up to ~5.03 μWh cm^{-2}, which is ~5 times higher than the oxygen plasma-treated symmetric carbon microelectrode-based electrochemical capacitor.

1. Introduction

The need for high-performance microscale energy storage units for rapidly growing microelectronic devices have continued to attract much attention [1]. Miniaturized batteries and electrochemical capacitors (ECs) are attractive candidates for on-chip energy storage application [2]. According to their energy storage mechanisms, ECs are based on electric double-layer capacitance (EDLC) or pseudocapacitance [3]. While EDLC involves charge storage through non-faradic adsorption/-desorption of electrolyte ions on the surface of electrode materials, pseudocapacitance mechanism involves surface or near-surface faradaic reactions of electrolyte ions with metal oxides or conductive polymer electrodes. Typically, ECs can give advantageous characteristics such as higher power density, faster charge/discharge properties, and ultralong cyclability than batteries.

However, the limited energy density of ECs represents a significant drawback [4]. Over the years, asymmetric ECs realized by the combination of EDLC and pseudocapacitive electrodes have been shown to be a promising strategy to achieve improved performance trade-off in terms of energy and power density due to enlarged cell voltage window [5–8]. Another interesting asymmetric device concept is based on the combination of the bulk and surface storage mechanisms enabled by a battery-type electrode and a capacitor-type electrode, respectively. Lithium-ion capacitor (LIC) is one of such systems, consisting of high energy battery-type electrode and high power capacitor-type electrode [9,10].

The electrochemical performance reports on LICs are mostly based on large cells which are not well suited for on-chip integration. On-chip LICs could potentially be favorable for integration along with other components in microelectronic devices to provide a good combination

* Corresponding author.
E-mail address: wangc@fiu.edu (C. Wang).

https://doi.org/10.1016/j.jpowsour.2020.227987
Received 13 October 2019; Received in revised form 10 February 2020; Accepted 29 February 2020
Available online 9 March 2020
0378-7753/

of high energy and power densities within limited footprint area. Recently, Li et al. reported a promising prototype on-chip LIC with lithiated graphite and activated carbon (AC) as the battery-type and capacitor-type electrodes, respectively, by injecting slurries of the electrode materials in an interdigital microchannel [11]. However, more facile and CMOS processing-compatible methods are desirable for the practical application of the on-chip LICs. In terms of device architecture, the fabrication of on-chip energy storage devices are targeted at ensuring high effective microelectrode surface area within a restricted space using scalable and facile approaches. 3D microelectrode designs offer higher effective surface area and better electrolyte accessibility than planar designs, which could result in enhanced areal capacity [12–16]. One of the most interesting 3D microelectrode fabrication approaches is the carbon microelectromechanical systems (C-MEMS) technique which generally involves photolithographic patterning and pyrolyzing photoresists in an inert atmosphere to obtain glassy carbon structures [17–20]. C-MEMS process is a facile route of obtaining a wide variety of ordered 3D carbon microelectrode structures with high resolution [17,21,22]. Various symmetric on-chip ECs with 3D carbon microelectrodes based on C-MEMS platform have previously been demonstrated [18,19,23]. It has been shown that the electrochemical properties of the carbon microelectrodes could be enhanced by introducing nanofeatures, for example, electrochemical activation [23], the incorporation of CNT [18], or by integrating pseudocapacitive materials such as polypyrrole (PPy) [19] and MnO_2 [20].

Given the prospects of providing enhanced areal capacity, the present study demonstrates a novel first generation 3D on-chip LIC based on C-MEMS-derived interdigital carbon microelectrodes. Our method involves subjecting the carbon microelectrode to oxygen plasma treatment to achieve improved capacitive properties as the capacitor-type electrode. The battery-type electrode in the LIC was realized by the integration of $LiFePO_4$ (LFP) on the 3D carbon microelectrodes by electrophoretic deposition (EPD). The carbon//LFP on-chip LIC evaluated using 1 M Li_2SO_4 aqueous electrolyte delivered an areal energy density up to ~5.03 μWh cm^{-2} which was ~5 times higher than symmetric carbon microelectrode-based EC. The on-chip LIC system could

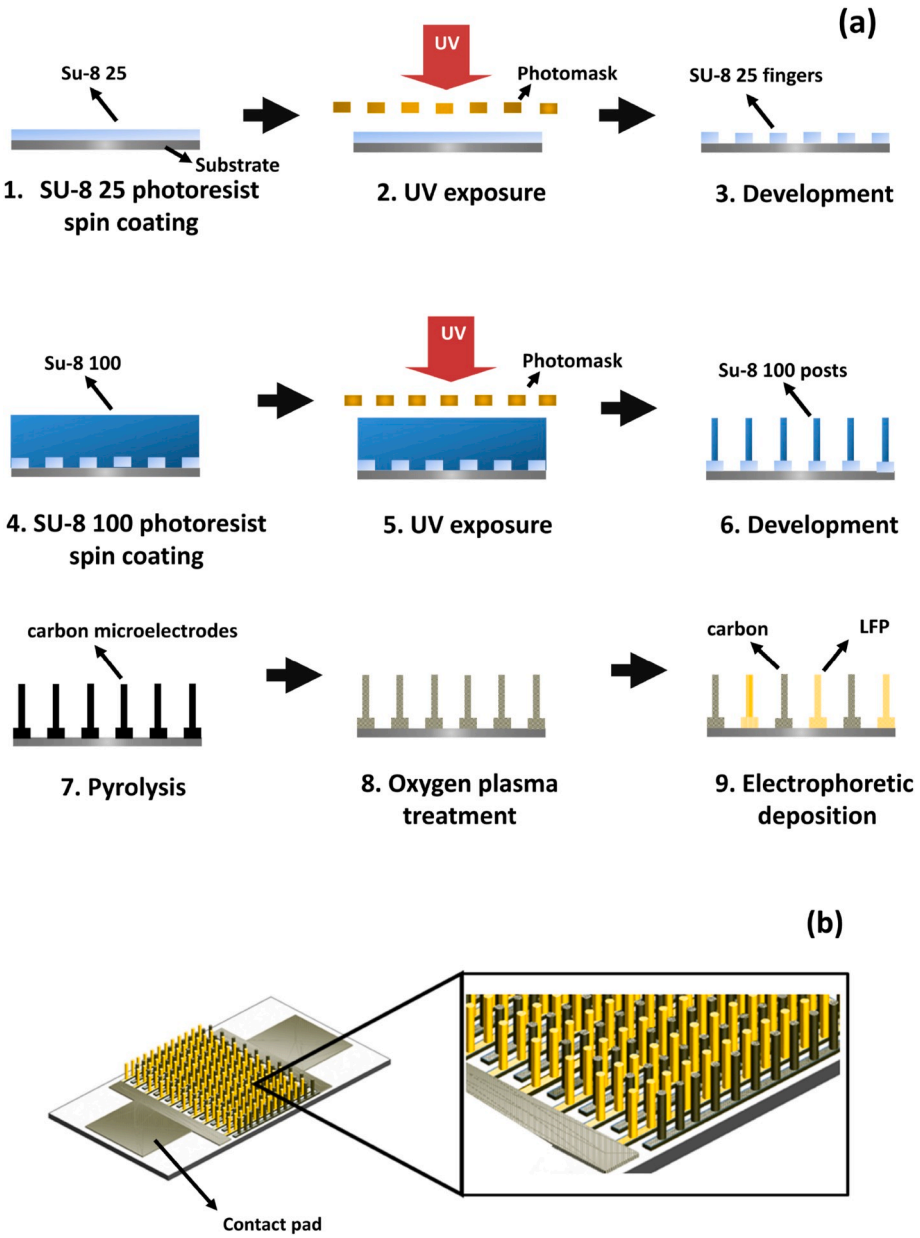

Fig. 1. (a) Illustration of the fabrication process of the C-MEMS-based on-chip LIC. (b) Schematic 3D view of the microdevice.

potentially be favorable in terms of facile fabrication approach and areal capacity for practical application in microelectronic devices. This study broadens the prospects of the application of C-MEMS technology beyond symmetric systems in the development of high-performance on-chip capacitive energy storage.

2. Experimental section

2.1. Interdigital carbon microelectrode arrays fabrication and LFP integration

An illustration of the C-MEMS-based on-chip LIC fabrication process is presented in Fig. 1a. First, a negative tone photoresist, SU-8 25 (MicroChem Corp.), was spin-coated on a 550 μm thick Si/Si_3N_4 (10, 000 Å) wafer at 500 rpm for 12 s and then at 3000 rpm for 30 s. The photoresist coated wafer was baked at 65 °C for 3 min and at 95 °C for 7 min on a hot plate. UV exposure through a photomask was then carried out using an OAI mask aligner with a dose of 300 $mJcm^{-2}$. Thereafter, a post-exposure bake was performed at 65 °C for 1 min followed by baking at 95 °C for 5 min. The resulting baked photoresist was developed to reveal a 2D interdigital finger pattern using a NANO™ SU-8 developer solution (MicroChem Corp.). In order to build an array of 3D structures on the 2D interdigital finger pattern, a second negative photoresist, SU-8100 (MicroChem Corp.), was spin-coated at 500 rpm for 12 s and then at 2000 rpm for 30 s, followed by baking (65 °C for 10 min, and 95 °C for 30 min) on a hot plate. The baked photoresist was patterned using a UV exposure dose of 700 $mJcm^{-2}$. Post-exposure bake (65 °C for 3 min and 95 °C for 10 min) was carried out followed by the development process to reveal the patterned photoresist using the SU-8 developer. The resulting samples were pyrolyzed by using a YFT 1700 tube furnace in a continuous flow of Ar (about 2000 sccm flow rate). The samples were initially heated at 350 °C (ramp 3 °C/min) for 30 min and then at 900 °C (ramp 5 °C/min) for 1 h, followed by natural cooling to room temperature in the Ar atmosphere. The interdigital patterned glassy carbon microelectrode devices obtained after the pyrolysis step were treated with oxygen plasma using a reactive ion etch (RIE) system (RIE-1701, MARCH) for 1, 5 and 10 min. An oxygen flow rate of 60 sccm, 400 mTorr pressure and 250 W power were used during the plasma treatment process. For LFP integration, both sides of the interdigital carbon microelectrode device were connected to the positive and negative sides of a DC power source for electrophoretic deposition (EPD) process. 18 mg commercial LFP powder comprising carbon coating purchased from MTI Corporation, 1.5 mg conductive agent (Super P Li) and 0.5 mg $MgCl_2$ as an EPD process additive [24], were dispersed in 20 ml acetone-water mixture (9:1 v/v) by ultrasonication for 4 min to obtain a suspension. The suspension obtained after ultrasonication was immediately used for EPD process by applying a constant voltage of 30 V for 5, 10 and 20 s. The devices fabricated were then washed several times with ethanol and dried overnight at 70 °C. A schematic 3D view of the on-chip microdevice is presented in Fig. 1b.

2.2. Characterization

Scanning electron microscopy (SEM) (JEOL 6330, Peabody, MA, USA) was used to reveal the surface of the carbon structures. The surface functionalities of the carbon microelectrodes were investigated by fourier transform infrared (FTIR) (JASCO FT/IR, 4100, Tokyo, Japan). Electrochemical evaluations were carried out with 1 M Li_2SO_4 aqueous electrolyte using a VMP3 multichannel potentiostat (VMP3, Princeton Applied Research). Electrochemical impedance spectroscopy (EIS) experiments were performed with frequency ranging from 1 MHz to 100 mHz. Cyclic voltammetry (CV) and galvanostatic charge-discharge (GCD) tests were carried out in a three-electrode setup using the oxygen plasma-treated carbon anode or LFP incorporated carbon microelectrode cathode as the working electrode, while a graphite rod and Ag/AgCl served as the counter and reference electrodes, respectively. The anode was evaluated within a voltage range of - 0.9 to 0.1 V, while the cathode was tested within - 0.3 to 0.6 V. CV and GCD tests were carried out on oxygen plasma-treated carbon//carbon symmetric devices as well as carbon//LFP hybrid devices in a two-electrode setup within a voltage range of 0–1.4 V.

3. Results and discussion

3.1. Materials characterization

The SEM image of a typical device and a single 3D carbon microelectrode obtained after the pyrolysis processes is presented in Fig. 2a and S1, respectively. An array of 3D carbon microelectrodes can be seen on top of planar interdigital carbon fingers. There are 20 interdigital fingers (10 for each electrode side) with length and width of about 4800 μm and 79 μm, respectively. The thickness of the fingers was about 15 μm. A typical device comprises 460 3D carbon microelectrodes (23 on each finger) with an average height of about 106 μm and diameter of about 46 μm. The total electrode geometric surface area of each side of the interdigital microelectrode (surface area of planar fingers and the projected 3D carbon structure) was ~0.07 cm^2. The device footprint area (planar area of the interdigital microelectrodes and the interspaces) was ~0.29 cm^2. The surface morphology of the as-prepared carbon electrode sample is shown in Fig. 2b. Oxygen plasma treatment resulted in roughening of the surface of the samples with the appearance of pits (Fig. 2c, d and 2e) because of the etching effect on the carbon material. The pits became larger with increasing plasma treatment duration from 1 to 10 min. The heights of the 3D carbon microelectrodes measured after the plasma treatment process were about 105, 104 and 96 μm for 1, 5, and 10 min treatment durations, respectively.

Fig. 3a shows the on-chip LIC with interdigital 3D microelectrodes comprising LFP electrode material and bare carbon. An enlarged view of the sample presented in Fig. 3b shows the LFP electrode material integrated on the 3D carbon microelectrode after EPD process, while Fig. 3c shows a bare 3D carbon microelectrode. Figs. S2a and S2b show the top-view SEM images of a carbon microelectrode after 5 min plasma treatment and after 10 s LFP integration deposition duration, respectively. Fig. 4a, b, 4c and 4d show the microelectrodes with increasing LFP electrode deposition durations. LFP electrode thicknesses of about 0.93, 1.19 and 2.90 μm for 5, 10, and 20 s deposition durations, were measured, respectively.

The surface functional groups produced after plasma treatment can be observed in the FTIR pattern shown in Fig. 5. An increase in the intensity of the functional group signals can be observed as plasma treatment duration increases. The broad peak at 3450 cm^{-1} is related to -OH groups of phenol or carboxylic functionalities [25], while the peak at 2930 cm^{-1} corresponds asymmetric stretching of the CH_2 functional groups [26]. The peaks at 1735 cm^{-1} can be assigned to C=O stretching of carboxyl group [27], while the 1610 cm^{-1} peak is related to C=C stretching of aromatic rings or C=O groups conjugated with aromatic rings [26]. Other peaks at 1502, 1237 and 1108 cm^{-1} are ascribed to, C=C stretching, C-O-C and C-O vibrations respectively [25,26,28].

3.2. Electrochemical evaluation

3.2.1. Carbon//carbon symmetric EC devices

The 5 min plasma-treated electrodes and untreated electrodes were examined as symmetric EC. The third cycle CV curves of carbon//carbon symmetric ECs before and after plasma treatment based on a two-electrode configuration at a scan rate of 1 Vs^{-1} are shown in Fig. 6a. The area under the CV curve of the treated sample is about 9 times larger than the untreated sample indicating improved charge storage behavior after plasma exposure [23]. The 5 min plasma-treated and the untreated ECs gave capacities of about 0.030 and 0.003 μAh cm^{-2} (normalized by device footprint area), respectively, at the 1 Vs^{-1} scan rate. Fig. 6b shows the third cycle CV curves of 5 min plasma-treated sample at

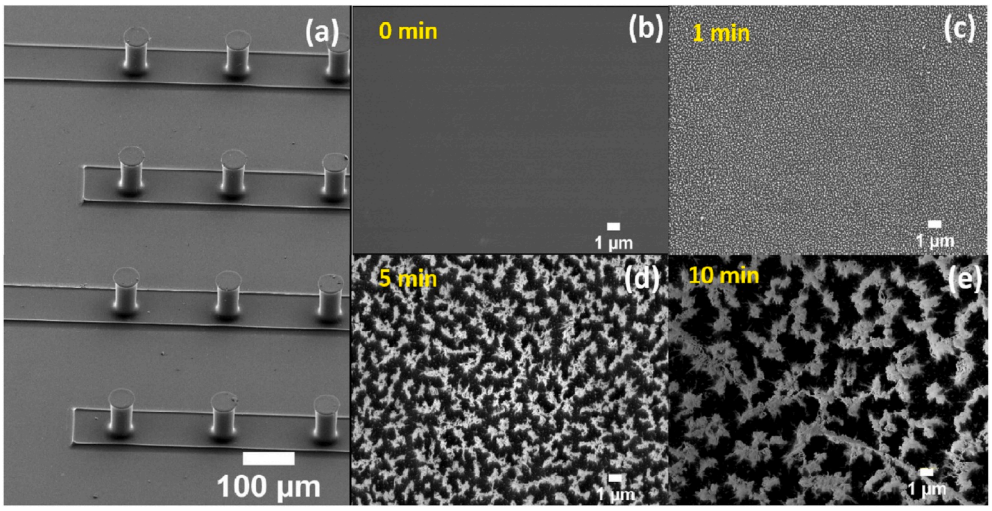

Fig. 2. (a) SEM image of interdigital 3D carbon microelectrodes. Surface morphology of the carbon microelectrodes with (b) 0 min, (c) 1 min, (d) 5 min and (e) 10 min oxygen plasma treatment durations.

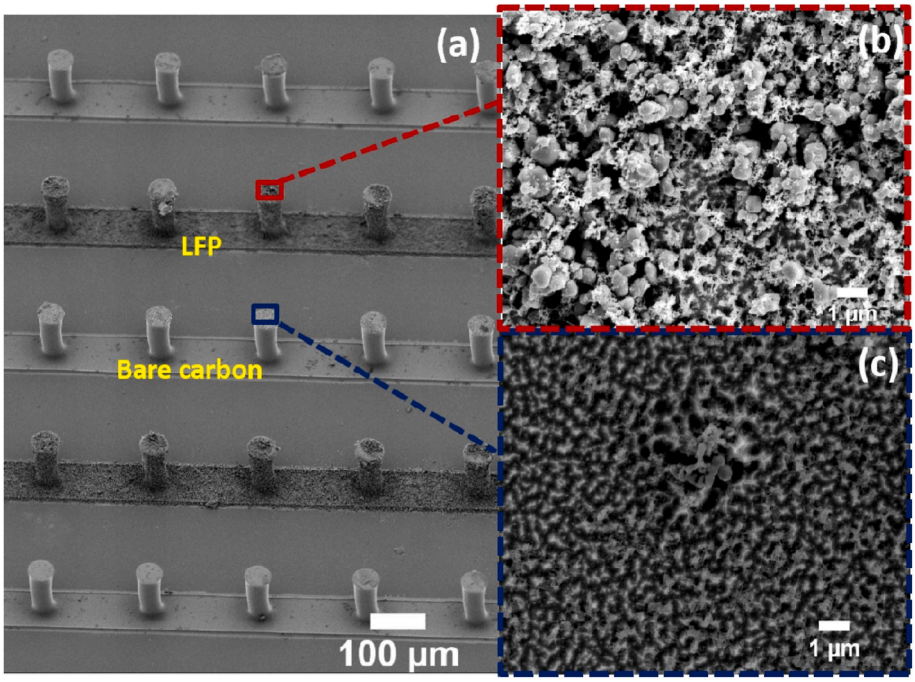

Fig. 3. (a) SEM image showing the on-chip LIC with interdigital 3D microelectrodes comprising LFP electrode material and bare carbon. An enlarged surface morphology of (b) LFP electrode material integrated on 3D carbon microelectrode after EPD process and (c) bare 3D carbon microelectrode.

different scan rates. The corresponding capacities calculated for 5, 10, and 20 Vs^{-1} were about 0.015, 0.010 and 0.008 μAh cm^{-2}, respectively, based on device footprint area. The enhanced capacitive performance can be attributed to the enlarged surface area as well as pseudocapacitance contribution from surface functional groups in the oxygen plasma-treated carbon material [23,29,30].

The GCD curves in the two-electrode test of the 5 min plasma-treated sample at 0.12 mA cm^{-2} for 10 cycles are presented in Fig. S3. The discharge capacity based on device footprint area calculated from the GCD curves of the sample was about 1.97 μAh cm^{-2} after the first cycle. A slightly lower discharge capacity of ~1.52 μAh cm^{-2} was obtained after the tenth cycle. The tenth cycle GCD curves of the devices at 0.36 mA cm^{-2} current density for different plasma treatment durations are presented in Fig. 7a. Among the devices, the 5 min plasma-treated sample gives the highest discharge capacity. The discharge capacities calculated from the GCD curves in Fig. 7a for 0, 1, 5, and 10 min plasma treatment durations were about 0.001, 0.041, 0.297 and 0.138, μAh cm^{-2}, respectively, based on device footprint area. The rate performance results presented in Fig. 7b also shows that the 5 min plasma-treated device gave the highest discharge capacities at different current densities. The discharge capacities after the tenth cycle for the 5 min plasma-treated sample at current densities of 0.24, 0.48 and 0.60 mA cm^{-2} were about 0.63, 0.18 and 0.13 μAh cm^{-2}, respectively, based on device footprint area. A discharge capacity of 1.32 μAh cm^{-2} was obtained when the current density was returned to the original of level of 0.12 mA cm^{-2} (after the tenth cycle) indicating that the initial capacity was fairly recovered after high current density test. Fig. 7c shows that the 5 min plasma-treated device gave the highest capacity after 200 cycles at a constant current density of 0.24 mA cm^{-2}. Discharge capacities of about 0.002, 0.060, 0.870 and 0.190 μAh cm^{-2} were obtained

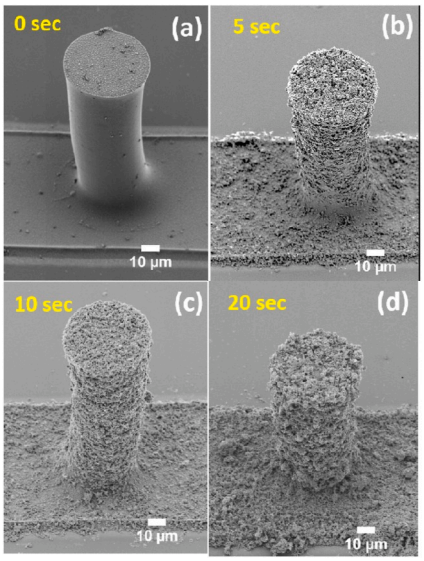

Fig. 4. SEM images of the interdigital 3D microelectrodes with (a) 0 s, (b) 5 s, (c) 10 s and (d) 20 s LFP deposition durations.

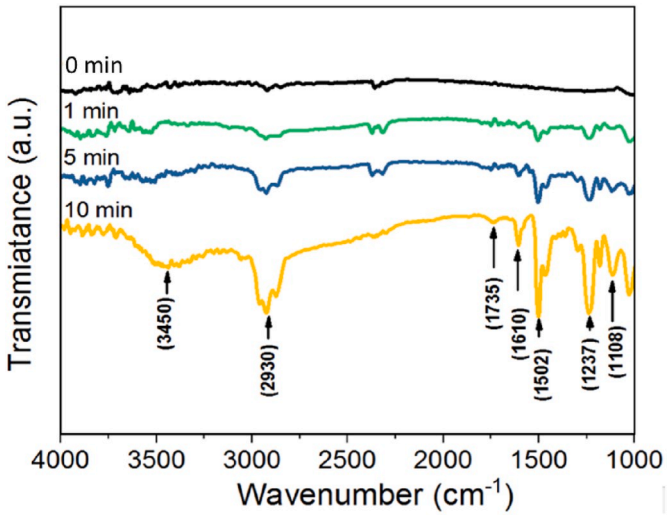

Fig. 5. FTIR pattern of C-MEMS-based carbon microelectrodes with different oxygen plasma treatment times.

for 0, 1, 5, and 10 min plasma-treated samples, respectively, at 0.24 mA cm^{-2} after 200 cycles.

The decreased discharge capacities of the device upon further increasing the oxygen plasma treatment duration from 5 to 10 min may be attributed to the reduced effective surface area of the interdigital microelectrodes. The average height of the 3D carbon microelectrodes reduced by 7.8% when the plasma treatment duration was increased from 5 to 10 min. Larger pores were also generated after the 10 min plasma treatment which may give lower specific surface area in the interdigital microelectrodes, leading to the lower discharge capacities observed. Another possible reason may be a reduced conductivity of the microelectrodes due to the functionalities induced by the oxygen plasma treatment [32]. The discharge capacities of the 5 min plasma-treated device normalized per total geometric surface area of individual microelectrode are 12.47, 4.93, 0.24, 0.14, 0.10 μAh cm^{-2} at current densities of 0.12, 0.24, 0.36, 0.48 and 0.60 mA cm^{-2}, respectively.

3.2.2. Carbon//LFP LIC devices

The on-chip LICs were fabricated with 5 min plasma-treated carbon microelectrodes as anode and LFP electrode material as the cathode. The electrochemical evaluation of the carbon microelectrode after 5 min plasma treatment and the LFP electrode in a three-electrode cell configuration is presented in Figs. S4 and S5, respectively. To achieve optimal electrochemical performance, the LFP electrode thickness was adjusted by controlling the EPD process duration. Fig. 8a shows the CV curves of a LIC device with 10 s LFP deposition duration at scan rates from 20, 50 and 200 mVs^{-1}. The nearly rectangular shape with the absence of obvious peaks on the CV curves indicate that capacitive behavior dominates in the device within a voltage range of 0–1.4 V. Fig. S6 shows the GCD curves of the first 10 cycles within this voltage range for a LIC with 10 s LFP deposition duration at a current density of 0.12 mA cm^{-2}. The discharge capacities obtained after the first and tenth cycles were about 8.36 and 7.29 μAh cm^{-2}, respectively, based on the device footprint area. Fig. 8b shows the tenth cycle GCD curves of the on-chip LIC with 5, 10 and 20 s LFP deposition durations at a current density of 0.36 mA cm^{-2}. The GCD curves signifies that the sample with 10 s LFP deposition duration gave the highest discharge capacity. The discharge capacities calculated from the GCD curves were respectively about 0.46, 3.33 and 0.76 μAh cm^{-2} for the on-chip LIC with 5, 10 and 20 s LFP deposition durations. The rate performance of the on-chip LICs with different LFP deposition durations is presented in Fig. 8c indicating that the on-chip LIC with 10 s LFP deposition duration showed the highest discharge capacities in all current densities. For example, at the highest current density of 0.60 mA cm^{-2} the devices gave discharge capacities of about 1.61, 0.35 and 0.16 μAh cm^{-2} for devices with 5, 10 and 20 s LFP deposition durations, respectively. Moreover, the on-chip LIC with 10 s LFP deposition durations gave a discharge capacity of about 7.64 μAh cm^{-2} after the current density was returned to the initial level of 0.24 mA cm^{-2}. However, some sharp capacity decrease can be observed at about the sixth and tenth cycles upon further cycling at this current density. This may be attributed to slight detachment of active materials or current collector fingers after being subjected to high current density. A discharge capacity of about 5.72 μAh cm^{-2} was obtained for the device after the tenth cycle at the 0.24 mA cm^{-2} current density. The energy-power density relationships of different on-chip hybrid devices are shown in the Ragone plots in Fig. 8d. The on-chip LIC with 10 s LFP deposition duration delivered the highest areal energy density with a maximum value of ~5.03 μWh cm^{-2} and a maximum areal power density of ~0.42 $mWcm^{-2}$. The maximum areal energy densities of the devices with 5 and 20 s LFP deposition durations were ~1.70 and 1.53 μWh cm^{-2}, respectively. The maximum areal energy density realized was about 5 times higher than the symmetric carbon//carbon EC which gave a maximum areal energy density of ~1.05 μWh cm^{-2}. The corresponding maximum volumetric energy and power densities of the on-chip LIC with 10 s LFP deposition duration was ~7.91 μWh cm^{-3} and 0.25 Wcm^{-3}, respectively. The cyclability of the on-chip LIC with 10 s LFP deposition duration at a constant current density of 0.24 mA cm^{-2} is presented in Fig. 8e. The capacity increased for the first 1–550 cycles and decreased sharply at about 550th cycle. The capacity further increased after the 560th cycle until the 1450th cycle where it sharply decreased again. Thereafter, an almost steady capacity (~3.67 μAh cm^{-2}) was maintained up to the 2000th cycle. The capacity increase observed at initial cycles may be due to electro-activation process in the electrode materials of the on-chip LIC [19,23,31]. Prolonged cycling may facilitate the improved accessibility of electrolyte to the active materials leading to capacity increase. Similar to the rate capability test result in Fig. 8c, the sharp capacity decrease in the cyclability curve may also be attributed to the gradual detachment of active materials and/or the carbon microelectrode with prolonged cycling. Optimizing the EPD parameters and pyrolysis process may improve the cycling stability of the LIC.

The on-chip LICs exhibit iR drop in the GCD curves presented in Fig. 8b. The iR drop correlates to the internal resistance of the cells including ohmic resistance (R_s), ionic resistance (R_i), solid electrolyte interface resistance (R_{SEI}) and charge transfer resistance (R_{ct}) [32]. The

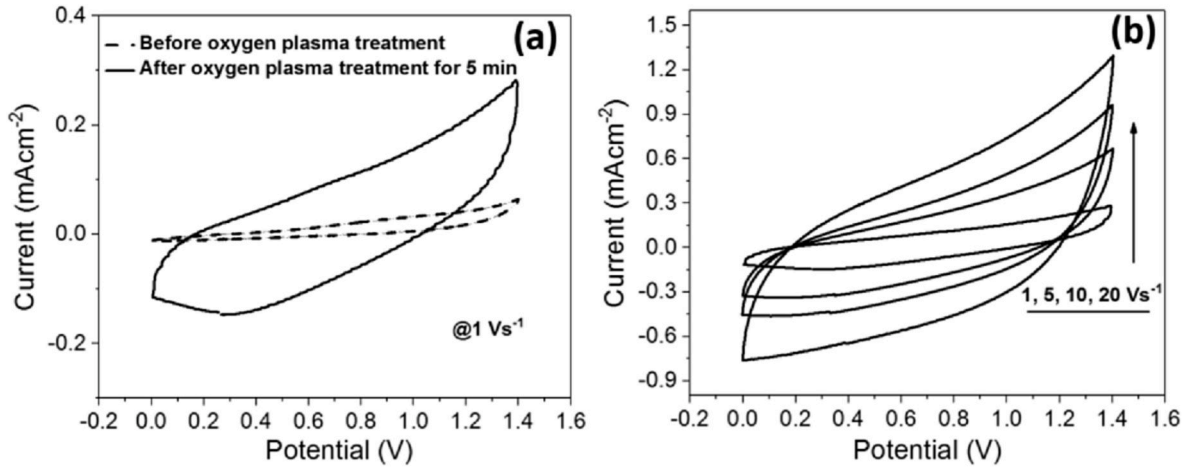

Fig. 6. (a) CV curves of symmetric ECs with 3D carbon microelectrodes before and after oxygen plasma treatment. (b) CV curves of EC with 3D carbon microelectrodes plasma-treated for 5 min at different scan rates.

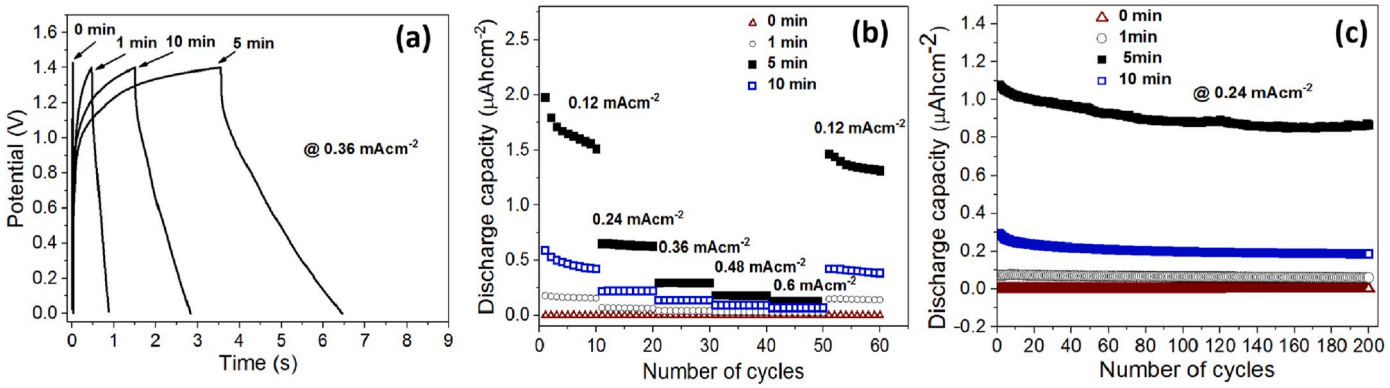

Fig. 7. (a) GCD curves of symmetric ECs with 3D carbon microelectrodes at different oxygen plasma treatment durations. (b) Rate capability of the ECs at different current densities. (c) Cycling performance of the ECs.

Nyquist plots of the on-chip LIC with different LFP deposition durations is presented in Fig. S7a to give insight into the electrochemical performance results observed. The plots consist of one depressed semicircle at the high frequency region and a sloping line at the low frequency region. The intercept of the plots correlates to the R_s, while the depressed semicircle may be related to the R_{ct} [32]. The sloping line in the low frequency region represents the impedance of electrolyte ion diffusion known as the Warburg diffusion (W_s) [33,34]. The cell with 20 s LFP deposition duration showed the largest suppressed semicircle in the Nyquist plot which may be attributed to high R_i in the cell. The R_i may be influenced by the resulting electrode porosity with prolonged LFP deposition durations. The LFP electrode structure after prolonged EPD process may exhibit the smallest pore structure distribution due to a dense packing of electrode material particles leading high ion transport resistance [35]. As presented in Fig. S7b, the Nyquist plots of the on-chip LIC before and after 2000 cycles also show one depressed semicircle at the high frequency region and a sloping line at the low frequency region. The cycled on-chip LIC exhibit significantly larger depressed semicircle indicating increased internal resistance and charge transfer resistance after cycling. The SEM images of the 3D carbon and LFP microelectrodes after 2000 cycles are presented in Fig. S8. The 3D structure of the electrodes is clearly retained without obvious cracks or peeling of the electrodes after cycling. The cycled LFP electrode particles appear loosened and slightly covered with surface film which may which may contribute to enhanced resistance observed in the Nyquist plot. The performance comparison of the on-chip LIC demonstrated in this work with other microscale ECs described in literature is presented in Table S1. We can see from Table S1 that the maximum volumetric energy density of our on-chip LIC exceeds some microscale symmetric and asymmetric ECs reported in literature. A high operating potential is one of the main requirements for high energy density in electrochemical energy storage systems. In this study, a maximum operating potential of 1.4 V was attained in contrast to the typical 1 V in aqueous electrolyte systems due to irreversible water hydrolysis at ~1.2 V. It has been previously described by other group that the Li_2SO_4 electrolyte salt employed in this study exhibit strong Li^+ and SO_4^{2-} solvation which may suppress water hydrolysis and expand the operation potential [36]. Our work is an initial full cell study on the application of C-MEMS technique for the development of on-chip LIC in aqueous electrolyte. Future efforts will include capacity and rate performance matching of the capacitor-type carbon microelectrode with the battery-type cathode to ensure optimal performance of the on-chip LIC system. It is also expected that improving the capacitive behavior of the carbon microelectrode, the incorporation of other battery-type electrode materials capable of providing faster kinetics or employing high voltage electrolytes would ensure higher energy-power density tradeoffs in the on-chip LIC system. The C-MEMS approach demonstrated in this study exhibits promising potential for the facile development of high-performance on-chip LICs with 3D microelectrodes.

4. Conclusion

We describe a novel on-chip LIC based on interdigital 3D carbon microelectrodes. The study explores the potential application of a high

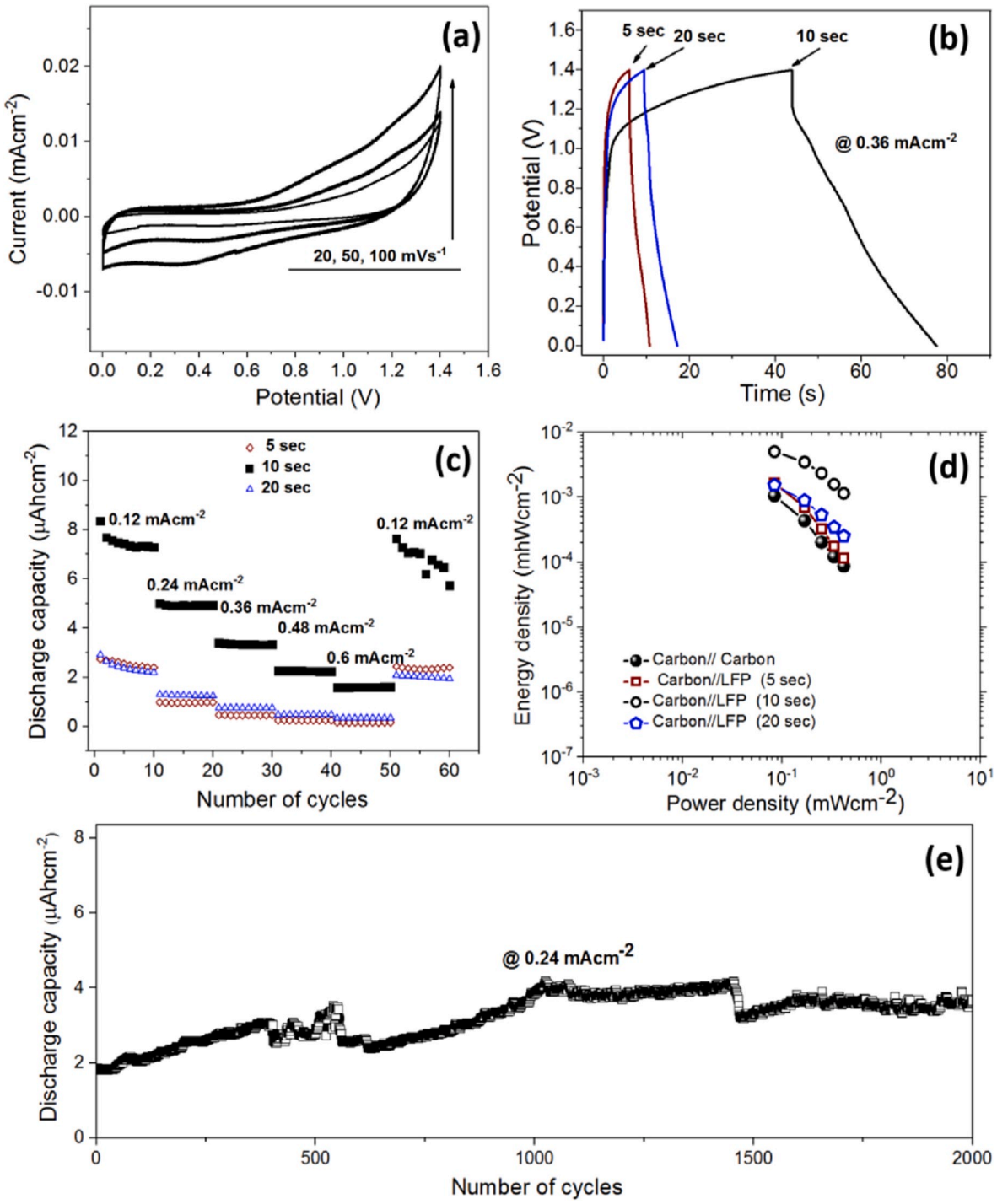

Fig. 8. (a) CV curves at different scan rates of LIC with 10 s LFP deposition duration. (b) GCD profiles, (c) rate performance and (d) Ragone plot of LICs with different LFP deposition duration. (e) Cycle performance of LIC with 10 s LFP deposition at a current density of 0.24 mA cm^{-2} for 2000 cycles.

aspect ratio 3D platform based on C-MEMS technology beyond symmetric on-chip ECs. Oxygen plasma-treated 3D carbon microelectrodes served as the capacitor-type electrode in the LIC, while LFP integrated on the carbon microelectrodes was used as the battery-type cathode. The carbon//LFP LIC delivered an areal energy density up to ~5.03 μWh cm^{-2}, about 5 times higher than symmetric 3D carbon microelectrode EC evaluated, which indicates the advantage of enhanced energy density by pairing a battery electrode with a double layer capacitor electrode in one cell with limited foot print area. The on-chip LIC could potentially be favorable as high-performance compact and integrable energy storage system for practical application in microelectronic devices.

Declaration of competing interest

The authors declare that they have no known competing financial interests or personal relationships that could have appeared to influence the work reported in this paper.

CRediT authorship contribution statement

Ebenezer Adelowo: Conceptualization, Methodology, Data curation, Formal analysis, Writing - original draft, Writing - review & editing. **Amin Rabiei Baboukani:** Data curation, Formal analysis, Writing -

review & editing. **Omena Okpowe:** Data curation, Formal analysis, Writing - review & editing. **Iman Khakpour:** Data curation, Formal analysis, Writing - review & editing. **Meer Safa:** Formal analysis. **Chunhui Chen:** Formal analysis. **Chunlei Wang:** Funding acquisition, Project administration, Writing - review & editing.

Acknowledgments

This work was partially supported by the National Science Foundation (NSF) projects (No. 1506640, No. 1509735 and No. 1611088) and Precise Advanced Technologies and Health Systems for Underserved Population (PATHS-UP) Engineering Research Center (ERC). The authors acknowledge Florida International University for support through a Dissertation Year Fellowship (DYF). C. Wang acknowledges the visiting professor fellowship from Alabama Transportation Institute at the University of Alabama.

Appendix A. Supplementary data

Supplementary data to this article can be found online at https://doi.org/10.1016/j.jpowsour.2020.227987.

References

[1] P. Huang, C. Lethien, S. Pinaud, K. Brousse, R. Laloo, V. Turq, M. Respaud, A. Demortière, B. Daffos, P.L. Taberna, B. Chaudret, Y. Gogotsi, P. Simon, On-chip and freestanding elastic carbon films for micro-supercapacitors, Science 351 (2016) 3717–3720, https://doi.org/10.1126/science.aad3345.
[2] M.F. El-kady, R.B. Kaner, Scalable fabrication of high-power graphene micro-supercapacitors for flexible and on-chip energy storage, Nat. Commun. 4 (2013) 1475–1479, https://doi.org/10.1038/ncomms2446.
[3] P. Simon, Y. Gogotsi, Materials for electrochemical capacitors, Nature 7 (2008) 845–854, https://doi.org/10.1038/nmat2297.
[4] J. Jiang, Y. Zhang, P. Nie, G. Xu, M. Shi, J. Wang, Y. Wu, Progress of nanostructured electrode materials for supercapacitors, Adv. Sustain. Syst. 2 (2018) 1700110, https://doi.org/10.1002/adsu.201700110.
[5] J.W. Long, D. Bélanger, T. Brousse, W. Sugimoto, M.B. Sassin, O. Crosnier, Asymmetric electrochemical capacitors — stretching the limits of aqueous electrolytes, MRS Bull. 36 (2011) 513–522, https://doi.org/10.1557/mrs.2011.137.
[6] H. Gao, F. Xiao, C.B. Ching, H. Duan, High-performance asymmetric supercapacitor based on graphene hydrogel and nanostructured MnO 2, ACS Appl. Mater. Interfaces 4 (2012) 2801–2810, https://doi.org/10.1021/am300455d.
[7] T. Brousse, B. Daniel, To Be or not to Be Pseudocapacitive ? J. Electrochem. Soc. 162 (2015) 5185–5189, https://doi.org/10.1149/2.0201505jes.
[8] Y. Shao, M.F. El-kady, J. Sun, Y. Li, Q. Zhang, M. Zhu, H. Wang, B. Dunn, R. B. Kaner, Design and mechanisms of asymmetric supercapacitors, Chem. Rev. 118 (2018) 9233–9280, https://doi.org/10.1021/acs.chemrev.8b00252.
[9] G.G. Amatucci, F. Badway, A. Du Pasquier, T. Zheng, An asymmetric hybrid nonaqueous energy storage cell, J. Electrochem. Soc. 148 (2001) A930–A939, https://doi.org/10.1149/1.1383553.
[10] D. Cericola, R. Kötz, Electrochimica Acta Hybridization of rechargeable batteries and electrochemical capacitors : principles and limits, Electrochim. Acta 72 (2012) 1–17, https://doi.org/10.1016/j.electacta.2012.03.151.
[11] S. Li, X. Wang, Micro Li-ion capacitor with activated carbon/graphite con figuration for energy storage, J. Power Sources 282 (2015) 394–400, https://doi.org/10.1016/j.jpowsour.2015.02.026.
[12] N.A. Kyeremateng, T. Brousse, D. Pech, Microsupercapacitors as miniaturized energy- storage components for on-chip electronics, Nat. Publ. Gr. 12 (2016) 7–15, https://doi.org/10.1038/nnano.2016.196.
[13] J. Pu, T. Zhang, J. Liu, High-energy-density , all-solid-state microsupercapacitors with three- dimensional interdigital electrodes of carbon/polymer electrolyte composite, Nanotechnology 27 (2015), 045701, https://doi.org/10.1088/0957-4484/27/4/045701.
[14] C. Shen, X. Wang, S. Li, W. Zhang, F. Kang, A high-energy-density micro supercapacitor of asymmetric MnO 2 e carbon con fi guration by using micro-fabrication technologies, J. Power Sources 234 (2013) 302–309, https://doi.org/10.1016/j.jpowsour.2012.10.101.
[15] C. Wang, G. Jia, L. Taherabadi, M. Madou, Wang, Chunlei Jia, Guangyao Taherabadi, Lili H. Madou, Marc J., A novel method for the fabrication of high-aspect ratio C-MEMS structures, Nanomaterials 14 (2) (2005) 348–358, https://doi.org/10.1109/JMEMS.2004.839312.
[16] C. Lethien, L. Bideau, Environmental Science micro-supercapacitors for powering the internet of things, Energy Environ. Sci. 12 (2019) 96, https://doi.org/10.1039/c8ee02029a.
[17] C. Wang, G. Jia, L.H. Taherabadi, M.J. Madou, A novel method for the fabrication of high-aspect ratio C-MEMS structures, J. Microelectromech. Syst. 14 (2005) 348–358, https://doi.org/10.1109/JMEMS.2004.839312.
[18] W. Chen, M. Beidaghi, V. Penmatsa, K. Bechtold, L. Kumari, W.Z. Li, C.P. Wang, A. Carbon, integration of carbon nanotubes to C-MEMS for on-chip supercapacitors, IEEE Trans. Nanotechnol. 9 (2010) 734–740, https://doi.org/10.1109/TNANO.2010.2049500.
[19] M. Beidaghi, C. Wang, Electrochimica Acta Micro-supercapacitors based on three dimensional interdigital polypyrrole/C-MEMS electrodes, Electrochim. Acta 56 (2011) 9508–9514, https://doi.org/10.1016/j.electacta.2011.08.054.
[20] R. Agrawal, E. Adelowo, A.R. Baboukani, M.F. Villegas, A. Henriques, C. Wang, Electrostatic spray deposition-based manganese oxide films — from pseudocapacitive charge storage materials to three-dimensional microelectrode integrands, Nanomaterials 7 (2017) 198, https://doi.org/10.3390/nano7080198.
[21] F. Galobardes, C. Wang, M. Madou, Investigation on the solid electrolyte interface formed on pyrolyzed photoresist carbon anodes for C-MEMS lithium-ion batteries, Diam. Relat. Mater. 15 (2006) 1930–1934, https://doi.org/10.1016/j.diamond.2006.08.015.
[22] H. Min, B.Y. Park, L. Taherabadi, C. Wang, Y. Yeh, R. Zaouk, M.J. Madou, B. Dunn, Fabrication and properties of a carbon/polypyrrole three-dimensional microbattery, J. Power Sources 178 (2008) 795–800, https://doi.org/10.1016/j.jpowsour.2007.10.003.
[23] M. Beidaghi, W. Chen, C. Wang, Electrochemically activated carbon micro-electrode arrays for electrochemical, J. Power Sources 196 (2011) 2403–2409, https://doi.org/10.1016/j.jpowsour.2010.09.050.
[24] N.A. Kyeremateng, M. Dinh, D. Pech, Electrophoretic deposition of Li4Ti5O12 nanoparticles with a novel additive for Li-ion microbatteries, RSC Adv. 5 (2015) 61502–61507, https://doi.org/10.1039/C5RA11039D.
[25] M. Domingo-Garcıa, F.J. Lopez-Garzon, M. Perez-Mendoza, Effect of some oxidation treatments on the textural characteristics and surface chemical nature of an activated carbon, J. Colloid Interface Sci. 240 (2000) 233–240, https://doi.org/10.1006/jcis.1999.6619.
[26] A. Shindo, K. Izumino, Structural variation during pyrolysis of furfuryl alcohol and furfural-furfuryl alcohol resins, Carbon N. Y. 32 (1994) 1233–1243.
[27] L.G. Nair, A.S. Mahapatra, N. Gomathi, K. Joseph, S. Neogi, C.P.R. Nair, Applied Surface Science Radio frequency plasma mediated dry functionalization of multiwall carbon nanotube, Appl. Surf. Sci. 340 (2015) 64–71, https://doi.org/10.1016/j.apsusc.2015.02.036.
[28] L. Lai, H. Yang, L. Wang, B.K. Teh, J. Zhong, H. Chou, L. Chen, W. Chen, Z. Shen, R. S. Ruoff, J. Lin, Preparation of supercapacitor electrodes through selection of graphene surface functionalities, ACS Nano 6 (2012) 5941–5951, https://doi.org/10.1021/nn3008096.
[29] Y. Joon, J. Joon, Y. Il, J. Kook, H. Na, J. Kim, S. Bin, Oxygen functional groups and electrochemical capacitive behavior of incompletely reduced graphene oxides as a thin-film electrode of supercapacitor, Electrochim. Acta 116 (2014) 118–128, https://doi.org/10.1016/j.electacta.2013.11.040.
[30] J. Niu, W.G. Pell, B.E. Conway, Requirements for performance characterization of C double-layer supercapacitors : applications to a high specific-area C-cloth material, J. Power Sources 156 (2006) 725–740, https://doi.org/10.1016/j.jpowsour.2005.06.002.
[31] H. Wang, Q. Hao, X. Yang, L. Lu, X. Wang, A nanostructured graphene/polyaniline hybrid material for supercapacitors, Nanoscale 2 (2010) 2164–2170, https://doi.org/10.1039/c0nr00224k.
[32] P.L. Moss, G. Au, E.J. Plichta, J.P. Zheng, Investigation of solid electrolyte interfacial layer development during continuous cycling using ac impedance spectra and micro-structural analysis, J. Power Sources 189 (2009) 66–71, https://doi.org/10.1016/j.jpowsour.2008.11.048.
[33] W.J. Cao, J.P. Zheng, Li-ion capacitors with carbon cathode and hard carbon/stabilized lithium metal powder anode electrodes, J. Power Sources 213 (2012) 180–185, https://doi.org/10.1016/j.jpowsour.2012.04.033.
[34] P. Pazhamalai, K. Krishnamoorthy, M.S.P. Sudhakaran, Fabrication of high-performance aqueous Li-ion hybrid capacitor with LiMn 2 O 4 and graphene, Chemelectrochem 4 (2017) 396–403, https://doi.org/10.1002/celc.201600550.
[35] C. Hitz, A. Lasia, Experimental study and modeling of impedance of the her on porous Ni electrodes, J. Electroanal. Chem. 500 (2001) 213–222.
[36] K. Fic, G. Lota, M. Meller, E. Frackowiak, Novel insight into neutral medium as electrolyte for high-voltage supercapacitors, Energy Environ. Sci. 5 (2012) 5842–5850, https://doi.org/10.1039/c1ee02262h.